 doi:10.20944/preprints202207.0443.v1

On the Surface Modification of LLZTO with LiF via a Gas-Phase Approach and the Characterization of the Interfaces of LiF with LLZTO as well as PEO+LiTFSI

Manuel Donzelli[a,b], Thimo Ferber[c], Vanita Vanita[b], Aamir Iqbal Waidha[b], Philipp Müller[c], Maximilian Mellin[c], René Hausbrand [c], Wolfram Jaegermann[c] and Oliver Clemens*[,b]

[a] *Technische Universität Darmstadt, Fachbereich Materialwissenschaft, Fachgebiet Materialdesign durch Synthese, Alarich-Weiss-Straße 2, 64287 Darmstadt, Germany.*

[b] *Universität Stuttgart, Institut für Materialwissenschaft, Chemische Materialsynthese, Heisenbergstraße 3, 70569 Stuttgart, Germany.*

[c] *Technische Universität Darmstadt, Fachbereich Materialwissenschaft, Fachgebiet Oberflächenforschung, Otto-Berndt-Straße 3, 64287 Darmstadt, Germany.*

*** Corresponding author:**

Prof. Dr. Oliver Clemens

Email: oliver.clemens@imw.uni-stuttgart.de

Fax: +49 711 685 51933

Preprints (www.preprints.org) | NOT PEER-REVIEWED | Posted: 29 July 2022 doi:10.20944/preprints202207.0443.v1

Abstract

In this study we present gas-phase fluorination as a method to create a thin LiF layer on $Li_{6.5}La_3Zr_{1.5}Ta_{0.5}O_{12}$ (LLZTO). We compare these fluorinated films with LiF films produced by RF-magnetron sputtering, where we investigated the interface between the LLZTO and the deposited LiF showing no formation of a reaction layer. Furthermore, we investigate the ability of this LiF layer as a protection layer against Li_2CO_3 formation in ambient air. By this we show that Li_2CO_3 formation is absent at the LLZTO surface after 24 h in ambient air supporting the protective character of the formed LiF films and hence could enhance the handling of LLZTO in air for battery production. With respect to the use within hybrid electrolytes consisting of LLZTO and a mixture of polyethylene oxide (PEO) and Lithium bis(trifluoromethanesulfonyl)imide (LiTFSI) we also investigated the interface between the formed LiF films and a mixture of PEO LiTFSI by X-ray photoelectron spectroscopy (XPS) showing decomposition of the LiTFSI at the interface.

Keywords

LLZTO; surface modification; interface stability; fluorination; XPS

Preprints (www.preprints.org) | NOT PEER-REVIEWED | Posted: 29 July 2022 doi:10.20944/preprints202207.0443.v1

1 Introduction

Solid-state batteries are currently investigated for their potential to be used together with metallic Li anodes to achieve high energy densities. They comprise the use of a solid electrolyte with high ionic conductivities and large electrochemical stability window. Li-conducting garnets such as $Li_7La_3Zr_2O_{12}$ (LLZO) [1] or $Li_{7-x}La_3Zr_{2-x}Ta_xO_{12}$ (LLZTO) [2] can be stable towards metallic Li [3], and are of interest to be used in combination with ion-conducting polymers within hybrid electrolytes, e. g., consisting of polyethylene oxide (PEO), lithium bis(trifluoromethanesulfonyl)imide, and LLZTO [4, 5]. One intrinsic problem of garnet materials originates from their high basicity, and they can react with traces of water and CO_2 forming Li_2CO_3 at the surface [6]. This can then act as a passivation layer, hindering the transport of Li ions between grains as well as the transfer to the active electrode materials [7]. In addition, the volume changes of this corrosion process are unfavourable, which can lead to ongoing degradation of the bulk material. Also for hybrid electrolytes, the high basicity can result in reactions at the direct interface [8], and reducing the surface reactivity while maintaining a conductive surface is a challenge to be overcome to successfully use this type of material.

Various methods have been proposed for the surface modification of garnet materials, ranging from dissolving $LiOH/Li_2CO_3$ via acid treatment [9, 10] to the deposition of lithium-free salts as thin passivation layers, which, though not being ion conductors themselves, do not block lithium ion transport (e. g. Al_2O_3 [11] or Sb_2O_3 [12]). Further, lithium halides (LiX, X = Cl, Br, I) [13] prepared by wet-chemical approaches have been reported to be functional coatings for garnets. Also LiF, which shows high thermal and chemical stability, was considered recently and showed excellent coating properties making garnet pellets well wetable with metallic lithium [14]. However, the method suggested by the authors required the use of high vacuum deposition, making it difficult to be scaled up. Furthermore, melting LiF directly onto the surface of a garnet pellet was suggested [5]. While the authors could show a beneficial effect on Li_2CO_3 formation and no detrimental effect on the Li-ion diffusion, this technique requires temperatures above the melting point of LiF (T_{melt} = 845 °C).

For syntheses of garnet materials, the lithium precursor is normally used in excess to compensate lithium losses during material synthesis. This difficulty in balancing the Li to La/Zr concentration precisely must

Preprints (www.preprints.org) | NOT PEER-REVIEWED | Posted: 29 July 2022 doi:10.20944/preprints202207.0443.v1

be considered as one origin for the existence of unfavourable Li-compounds at the surface. Transformation of this residue to LiF as well as slightly degrading the garnet surface by using a mild gas-phase based fluorination might therefore provide a promising route to functional and stable garnet surfaces.

Most fluorination agents are either highly corrosive (e. g. anhydrous HF) or can lead to extended material degradation. An alternative lies in providing HF in low concentrations by decomposition of fluorine containing polymers such as PVDF [15], and this was used for topochemical fluorinations of powders or thin films, for the latter either by coating the polymer on top of the film or by heating it separately at ~ 200 °C which causes the evaporation of shorter polymer molecules which can then decompose at the surface directly [16, 17]. PVDF-based gas fluorination routes thus work by the partial release of HF species at the substrate surface.

Consequently, we suppose that this method could in principle function to transform surface-contaminating alkaline materials such as carbonates or hydroxides according to

$OH^- + HF \rightarrow H_2O + F^-$ or

$CO_3^{2-} + 2\ HF \rightarrow H_2O + CO_2 + 2\ F^-$

while maintaining a low acidity via a low *p*(HF).

In this work, we report on the use of a gas-phase fluorination route for the surface protection of garnet-type LLZTO films with the thin layers of LiF. We show that the method is suitable to protect thin films with flat surfaces from degradation to Li_2CO_3 under ambient conditions, while not reducing the conductivity significantly. In addition, we address the limitations of this method, showing that it has limitations with respect to the gas-streaming profile in order to surface protect porous geometries. In the second part, due to relevance of LiF coatings within composite electrolytes, we provide a detailed analysis of the interface between LLZTO and sputter-deposited LiF, as well as between LiF and stepwise deposited PEO/LiTFSI, complementary to our previous study of the interface between LLZTO and PEO/LiTFSI [8].

Preprints (www.preprints.org) | NOT PEER-REVIEWED | Posted: 29 July 2022 doi:10.20944/preprints202207.0443.v1

2 Experimental section

2.1 LLZTO thin film deposition

$Li_{6.5}La_3Zr_{1.5}Ta_{0.5}O_{12}$ (LLZTO) thin films were deposited by LASER-assisted chemical vapor deposition (LA-CVD) on Si wafers (CrysTec GmbH) with an orientation of (100). For a detailed description of the deposition setup please see previous publications of our group [18]. As precursors, 2,2,6,6-tetramethyl-3,5-heptanedionato lithium ($LiC_{11}H_{19}O_2$, STREM Chemicals GmbH, 98%), lanthanum(III) acetylacetonate hydrate ($La(C_5H_7O_2)_3 \cdot 4H_2O$, abcr GmbH, 99.9%), tantalum(V) tetraethoxyacetylacetonate ($TaC_{13}H_{27}O_6$, STREM Chemicals GmbH, 99.99%), and zirconium(IV) acetylacetonate ($Zr(C_5H_7O_2)_4$, STREM Chemicals GmbH, 98%) were mixed in stoichiometric ratio, with a 50 wt % excess of Li. As process gases Argon (1.45 slm, Air Liquide, 99.999%) and oxygen (1.0 slm, Air Liquide Deutschland GmbH, 99.999%) were mixed and used during the 15 min deposition step, together with a substrate temperature of 923 K. A 15 min annealing step under the same gas atmosphere and temperature was added after synthesis. In to get rid of carbon surface contaminations that originate from the use of carbon-rich precursor materials an additional annealing step was added. Thus, the synthesized films were subjected to 923 K for 1 h under ultrahigh vacuum conditions ($\sim 10^{-7}$ Pa) to remove these contaminations.

2.2 LiF coating via gas-phase fluorination

Surface fluorination of LLZTO films was performed by decomposing 2 g of polyvinylidene fluoride (PVDF) in a tube furnace under Argon atmosphere with an Argon gas flow of $Q = 1\ slm$ and a temperature of 240 °C. The sample was transferred into the already heated tube furnace, kept at 240 °C for 5 minutes and then taken out of the furnace directly into a glovebox with Argon atmosphere (Air Liquide, 99.999%) for cool down. The LLZTO thin films are placed in the gas stream behind the PVDF, so by decomposing PVDF small amounts of HF can reach the LLZTO surface, where the HF can then subsequently react with the surface contaminations like Li_2CO_3 or the also detected LiOH

$$Li_2CO_3 + 2\ HF \rightarrow 2\ LiF + CO_2 + H_2O$$

$$LiOH + HF \rightarrow LiF + H_2O$$

Preprints (www.preprints.org) | NOT PEER-REVIEWED | Posted: 29 July 2022 doi:10.20944/preprints202207.0443.v1

The residuals are carried away by the argon gas stream. Two samples were prepared by coating LLZTO via gas-phase fluorination in order to check for influences of the fluorination time. The two time steps were done with 5 min and 15 min respectively. Although prepared under UHV conditions and therefore free of Li_2CO_3 the films still have some LiOH impurities on the surface, as the XPS investigations revealed. Furthermore, the transport to the tube furnace was done under Argon, but during the insertion into the furnace the thin films were exposed to air and thus small amounts of Li_2CO_3 and LiOH could form.

2.3 LiF thin films via sputtering

LiF films prepared by sputtering have been done using a RF-magnetron sputter process with a commercial LiF target (*Alineason Materials Technology GmbH*) at a pressure of $p = 5 \cdot 10^{-1}\ Pa$ and an Argon gas flow of $Q = 10\ sccm$.

2.4 PEO and LiTFSI evaporation

For the deposition of thin films of poly(ethylene oxide) (PEO) and lithium bis(trifluoromethanesulfonyl)imide (LiTFSI) via physical vapour deposition, thermal co-evaporation from two independent sources is used. Each source consists of a self-made Knudsen cell with an electrically heated Al_2O_3 crucible. The PEO source is located directly under the garnet substrate, and the LiTFSI source is positioned at 45° to the PEO source at a distance of around 14 cm from the garnet film. PEO (2000 g/mol, Alfa Aesar) and LiTFSI (Sigma-Aldrich) are used. Both PEO and LiTFSI are vacuum-dried at 10^{-6} Pa for at least 24 h prior to use. Evaporation is performed with an external temperature of the crucible at $T_{crucible}$ = 483 K for PEO and $T_{crucible}$ = 518 K for LiTFSI at a pressure between 10^{-5} and 10^{-6} Pa.

2.5 LLZTO pellet preparation

LLZTO powders with the nominal composition similar to that of thin films were prepared via the conventional solid state synthesis route. Stoichiometric amounts of Li_2CO_3 (Thermo Fisher, >99.9%), La_2O_3 (Sigma-Aldrich, >99.9%), ZrO_2 (Sigma-Aldrich, >99%), Ta_2O_5 (Alfa Aesar, >99.9%) were weighed and hand-milled together with mortar and pestle. A 20 % excess of Li_2CO_3 was added to compensate for the lithium loss during sintering. Before use, La_2O_3 was dried at 1100 °C for 24 hours to remove any moisture. The mixture was first calcined at 900 °C for 8 hours at the heating and cooling rate of 3 °C/min.

Preprints (www.preprints.org) | NOT PEER-REVIEWED | Posted: 29 July 2022 doi:10.20944/preprints202207.0443.v1

After this first heating cycle, the materials were ground again and 20 % of Li_2CO_3 was added again to compensate for lithium loss at high temperatures. The powders were then pressed into pellets by applying a pressure of 2 tons for a minute followed by heat treatment at 1120 °C for 12 hours with the heating and cooling rate of 3 °C/min under the ambient atmosphere. The obtained LLZTO pellets were then removed from the furnace at 500 °C and transferred to an Ar-filled glove box to minimize exposure to the environment.

2.6 X-ray Photoelectron Spectroscopy (XPS)

XPS measurements have been performed in a *PHI Versaprobe 5000* spectrometer by *Ulvac-phi Inc*. with monochromatised Al Kα radiation (hv = 1486.6 eV), a spot size of d = 200 µm and a power of P= 50 W. Pressure in the measurement chamber was around $p = 10^{-7}\ Pa$. Survey spectra were collected with a pass energy of $E_{pass} = 187.85\ eV$ and a step size of $E_{step} = 1.0\ eV$, while detailed spectra were collected with a pass energy of $E_{pass} = 23.5\ eV$ and a step size of $E_{step} = 0.1\ eV$. The angle between sample and analyzer was, if not stated else, at $\theta = 45$ °. Interface experiments were performed by applying only slight amounts of material to the surface and then transferring the sample in situ to the XPS machine without breaking the vacuum for the subsequent measurements. This procedure was repeated until a covering film could be achieved and no substrate signal could be seen in the XPS anymore.

2.7 X-ray diffraction (XRD)

XRD patterns were recorded with a Rigaku Smartlab device with a HyPix-3000 detector in Bragg-Brentano geometry with a Cu Kα source operated at 40kV and 30 mA. The scan was performed from 15 ° to 30 ° (the short range was used to minimize the measurement time, in order to prevent degradation due to air leakages, but is sufficiently large to identify impurity phases according to our experiences) with a step size of 0.005 ° and a fixed divergent slit with 0.3 °. Due to the air sensitive nature of the measured thin films airtight sample holders were used. Refinements were performed with the TOPAS V6 (Bruker AXS, Germany) software.

Preprints (www.preprints.org) | NOT PEER-REVIEWED | Posted: 29 July 2022 doi:10.20944/preprints202207.0443.v1

2.8 Electrochemical impedance spectroscopy

Alternating current (AC) electrochemical impedance spectroscopy was carried out to characterize the conductivity of the as-synthesized and surface treated LLZTO pellets. The pellets were sputtered with a thin layer of gold on both sides for electronic contacting. The impedance measurements were carried out in the temperature range of 30 °C to 100 °C using the ITS unit (Biologic) connected to a MTZ-35 impedance analyzer by applying an AC signal of 100 mV amplitude with the frequency ranging from 1 MHz to 100 mHz. Fitting of the data was performed using RelaxIS (rhd instruments, Germany).

Preprints (www.preprints.org) | NOT PEER-REVIEWED | Posted: 29 July 2022 doi:10.20944/preprints202207.0443.v1

3 Results and discussion

3.1 Surface Modification and Protection of LLZTO thin films via a gas-phase fluorination approach

The garnet films of nominal composition of $Li_{6.5}La_3Zr_{1.5}Ta_{0.5}O_{12}$ could be obtained via laser-assisted chemical vapour deposition, similar to what was reported previously [19, 20]. The advantage of this method for surface analysis originates from the fact that high purity garnet films with smooth surfaces suitable for subsequent surface-sensitive analysis methods can be obtained, which showed suitable for various interface studies before [3, 8]. The phase purity of the garnet film was confirmed via the Rietveld analysis of X-ray diffraction of data (see Figure S 1).

To attempt a novel preparation route for surface fluorination under LiF formation, the films were placed inside a tube furnace, which was quickly heated to 240 °C, held at this temperature for 5 min, and quickly cooled afterwards, all under a flow of argon (99.999 % purity). A PVDF-filled boat was placed in front of the LLZTO films (with respect to the flow direction) as shown in Figure 1.

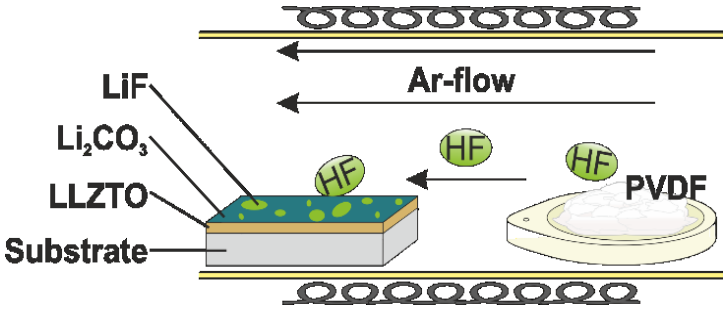

Figure 1. Schematic synthesis setup for the gas-phase fluorination.

X-ray photoelectron spectroscopy was used to analyse the surface of the LLZTO films. A strong signal of F can be detected at the surface (Figure 2a). Remarkably, no carbon species apart from adventitious carbon (resulting from air exposure) could be found at the film surface, indicative for the HF-based fluorination mechanism. The formed LiF layer shows an approximate composition of $Li_1F_{1.04}$ in XPS measurements confirming that fluoride mainly exists at the surface in a stoichiometric composition (Figure 2b)). Apparently, also specific

Preprints (www.preprints.org) | NOT PEER-REVIEWED | Posted: 29 July 2022 doi:10.20944/preprints202207.0443.v1

signals from the underlying garnet, such as the La3d and Zr3d peaks, as the most intense signals of LLZTO, are still detectable. Additionally, the ratio of La:Zr was determined from XPS to be 66.6:33.4, still matching well with the composition of the garnet material. The overall intactness of the garnet film could also be confirmed by XRD analysis, confirming insignificant decomposition of the garnet as well as the absence of reflections belonging to LiF, which layer thickness is far too low to be detected by this method (Figure S 1). Due to the surface sensitive character of the XPS measurement with an information depth below 10 nm, this implies that the formed layer of LiF must be very thin, in the range of a few atomic layers, or incompletely covering the surface. We further note that the exposure time to PVDF does seem to have a strong influence on the thickness of the LiF layer. After tripling the exposure time, the La/Zr/Ta LLZTO signals can't be detected by XPS anymore (Figure S 2).

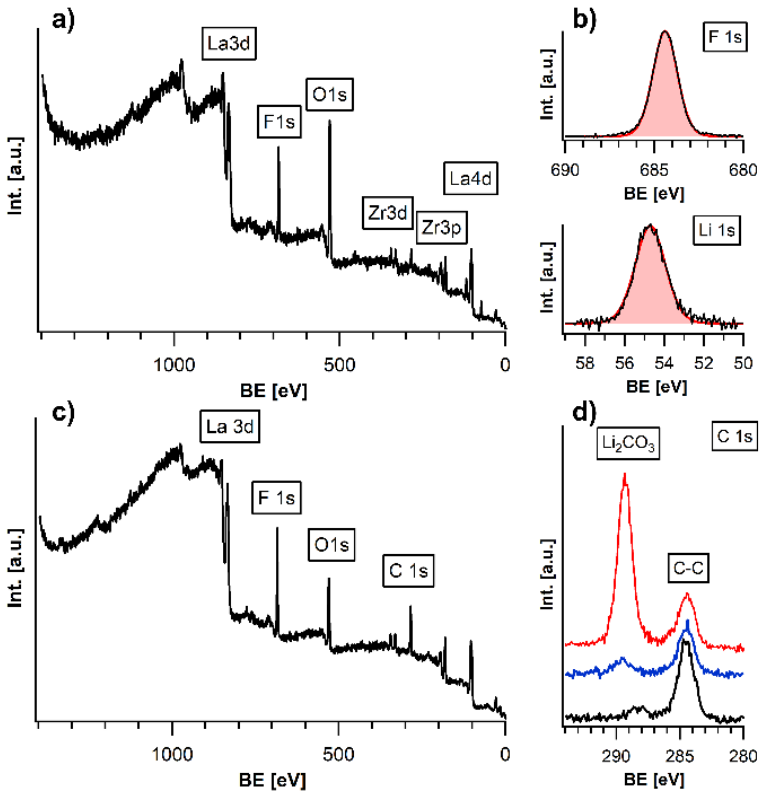

Figure 2. a) XPS survey spectrum of gas-phase fluorination LiF coated LLZTO b) Detailed Li1s and F1s spectra of gas-phase fluorination LiF coated LLZTO c) XPS survey spectrum of gas-phase fluorination LiF coated LLZTO after 24 h in ambient air d) Comparison of the detailed XPS C1s emission lines of an uncoated LLZTO (red), sputter-coated LLZTO (blue) and gas-phase fluorinated LLZTO (black).

In order to compare the gas-phase fluorination approach to other surface modification techniques, we use a sputtered LiF film as comparison. Thus, we compared gas-fluorinated films to LiF-sputtered films with respect to their surface composition as well as their behaviour

 doi:10.20944/preprints202207.0443.v1

on air exposure. Also for the LiF sputtered films, the resulting Li:F ratio of 50:50 confirms the presence of LiF at the surface, while La and Zr from the underlying substrate are still detectable (Figure S 3). Comparing the two methods, the gas-phase fluorination is advantageous regarding the required reaction time (5 min vs. 120 min) as well as the fact that no high vacuum equipment is needed.

In order to examine the protective character of the LiF and to determine the degree of coverage, the different LiF-coated LLZTO films were exposed to ambient air for 24 h and compared to an un-coated film. For the latter, a strong signal corresponding to Li_2CO_3 at 289.55 eV [21] can be found in the C1s spectrum (next to the signal of adventitious carbon, which originates from the need to remove the film from UHV conditions), as is expected due to the strong basicity of the material on exposure to CO_2/H_2O. Furthermore, no signals of the heavy elements can be detected at the surface, showing ongoing degradation due to the absence of surface passivation (see Figure S 5 and Figure 2d). In contrast, the gas-phase fluorinated film shows no degradation of the LiF-layer and the LLZTO layer underneath after exposure to air. For the LiF-coated films, all characteristic peaks of the LLZTO are still detectable in the XPS survey spectrum (Figure 2c)). On comparing the detail spectrum of the C1s emission line, the gas-phase fluorinated sample didn't show signs of a carbonate signal, whereas the surface-sputtered film showed a small signal belonging to Li_2CO_3 (Figure 2d). The increased surface stability to ambient conditions can be well explained by the low basicity of LiF as compared to highly basic LLZTO, which reacts with acidic compounds such as H_2O/CO_2. Further, it can be concluded that the gas-phase fluorinated films possess a close to full surface coverage, whereas the sputtering can easily lead to partially incomplete covering due to shadowing effects possibly induced by a small roughness of the synthesized LLZTO films.

In addition, attempts were made to study the influence of the LiF coating on the Li-ion conductivity by electrochemical impedance spectroscopy. Applying this technique to thin films is an experimental challenge. We emphasize that it was not possible to conduct this study with the LLZTO thin films due to the use of non-conducting SiO_2 substrates, which would only allow for in-plane measurements with an unfavourable surface to volume ratio to determine the

Preprints (www.preprints.org) | NOT PEER-REVIEWED | Posted: 29 July 2022 doi:10.20944/preprints202207.0443.v1

influence of the LiF coating. Further, the use of alternative conducting substrates such as Pt results in the formation of Li_2PtO_3 at the Pt to garnet interface, which possess an impedance signature [19] and would overlap with additional surface layer impedances from surface fluorination.

To avoid these effects and to facilitate evaluation of the impedance data, we transferred the developed fluorination method to a series of sintered garnet pellets with the theoretical densities of ~ 74 %. By this we attempted to investigate as prepared pellets to pellets which were fluorinated on both sides. In addition, both fluorinated and non-fluorinated pellets were left standing outside the glovebox for ~ 1 day to induce humidity and CO_2 related degradation in order to develop some understanding on the morphology of the fluorinated surface. A comparison of the as-recorded impedance data is shown in Figure 3 (exemplary fits of the impedance data are shown in Figure S 7, the corresponding equivalent circuit models are shown in Figure S 8.

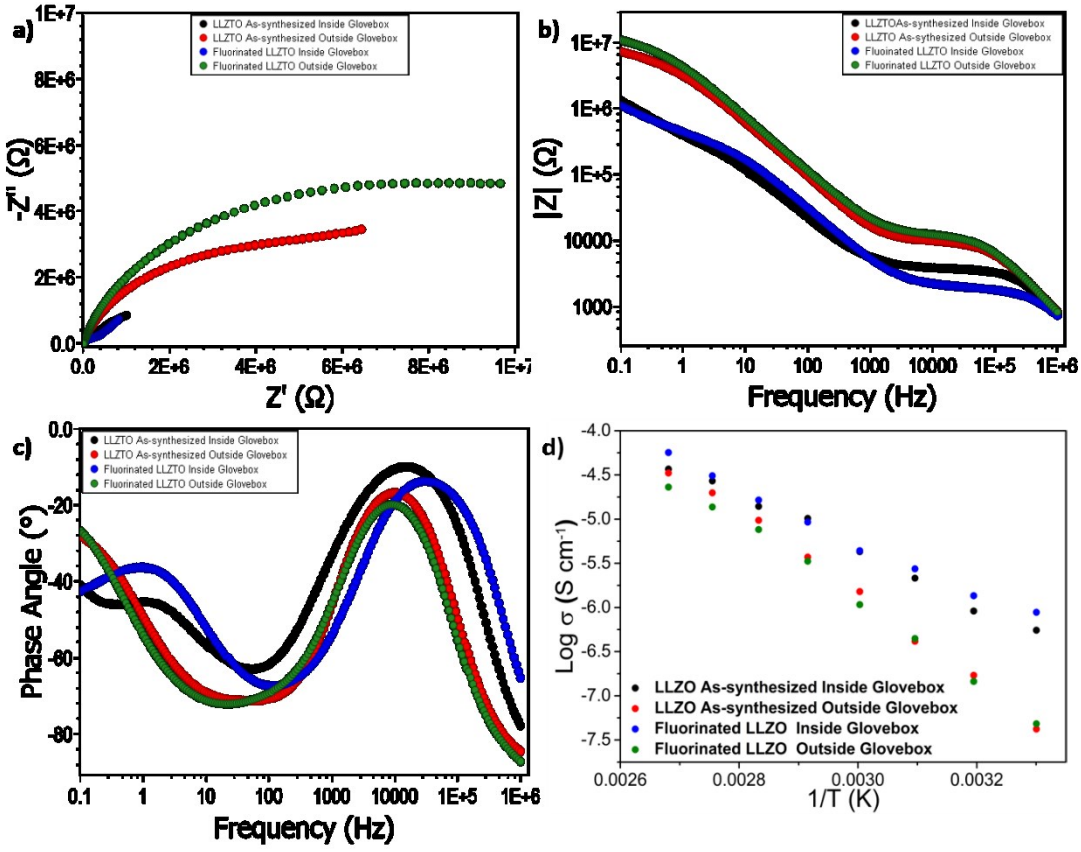

Figure 3. Comparison of the a) Nyquist b &c) Bode plots of the as-synthesized and fluorinated LLZTO pellets kept inside and outside of the argon filled glovebox. d) Arrhenius plots for the same samples measured in the temperature range of 30 °C and 100 °C.

Preprints (www.preprints.org) | NOT PEER-REVIEWED | Posted: 29 July 2022 doi:10.20944/preprints202207.0443.v1

XRD analysis (which characterizes the first 100 µm of the pellet surface at maximum) shows that the fluorination is not impacting the bulk structure of the garnet materials (see Figure S 6). From the Nyquist and Bode plots in Figure 3a-c as well as the evaluation of the temperature dependency (see Figure 3d), one can derive some information on the impact of the fluorination reaction on functional properties. Remarkably, there is no indication of a clear separate semicircle appearing for the fluorinated comparing to the non-fluorinated sample. Thus, we conclude that the fluorination reaction does not result in a degradation of the underlying garnet material and that the LiF is likely to be present at the surface only. Further, this surface layer can be expected to be thin and not impede the conductivity significantly more than surface phases originating from small off-stoichiometries at the surface obtained after garnet synthesis would do anyways. This can be brought in well agreement with the XPS spectra discussed in the previous section, which show that the surface layer formation of LiF via a gas-phase approach requires a well-adjusted reaction time, but can then lead to transformation of surface species to LiF without destruction of the underlaying garnet phase.

In addition, the impedance study shows that though the LiF surface layer is stable under ambient condition, it cannot protect degradation of the garnet from gas-phase degradation fully, if the substrate shows high porosity. This can be understood regarding the fairly low density of the pellet of ~ 74 % of the theoretical density (see Figure S 6 for the XRD patterns of the pellets). This indicates that though the method is suitable to modify surfaces, the streaming profile within the tube furnace might be unfavourable for protecting inner pores fully from interaction with H_2O/CO_2. Thus, applying this method to modify porous LLZTO pellets before infiltration with PEO+LiTFSI needs to be elaborated further [22].

3.2 Analysis of the Stability of the LLZTO and PEO/LiTFSI interfaces towards LiF

Due to the potential of LLZTO be used in combination with polymer electrolytes such as PEO/LITFSI, we further characterized the potential existence of reaction layers between LLZTO as well as PEO/LiTFSI with LiF at the interface. Such reaction layers can have an

Preprints (www.preprints.org) | NOT PEER-REVIEWED | Posted: 29 July 2022 doi:10.20944/preprints202207.0443.v1

important impact on functional properties in case of formation of unfavourable side phases which might hinder lithium ion migration by passivating phases. Due to the fact that the gas-phase fluorination route cannot control the thickness of the LiF layer, these experiments had to be performed on sputter-coated films, which allow for adjusting the thickness of LiF stepwise.

The XP spectra of the as-prepared LLZTO substrate show the typical LLZTO emission lines without any Li_2CO_3 contamination (Figure 4). Overall, the XP spectra resemble in shape and position to previously shown LLZTO spectra from our group [8]. After the annealing process the surface of the LLZTO is completely free of any carbon contamination (Figure S 5), which may be present after the synthesis, only a small amount of LiOH is present. None of the La3d, Zr3d or the Ta4f emission lines do show any sign of reduction from the annealing nor any other unexpected oxidation state. With the sputter deposition of t = 2 min of LiF, the F1s spectrum shows only the emission line of LiF at its typical binding energy of E_B = 684.7 eV [23, 24]. While the shape of all LLZTO emissions does not change upon LiF deposition it comes to an overlap of the La3d emission line with the fluorine KLL Auger line of the LiF between E_B = 825 and 840 eV [25]. In the O1s and the Zr3d spectrum no new emission line can be observed, but only the damping of the LLZTO and LiOH intensity, while the Li1s spectrum now exhibits the Li1s emission line of LiF at E_B = 55.0 eV. The Ta4f lines are damped as well and the appearance of the F2s line of the LiF at E_B = 28.9 eV can be seen. Upon increase of the LiF deposition time to t = 32 min, the same trend as for t = 2 min can be observed. This continues up to t = 512 min, where no LLZTO emission line can be detected in the spectra anymore. Only the emission lines of Li and F are present and the missing O1s spectrum demonstrates the complete absence of any oxygen as well. During the deposition, both, the LLZTO and the LiF emission lines undergo a binding energy shift (Figure 4b)). This can be attributed to intercalation of Li ions into the LLZTO at the beginning of the LiF deposition. A detailed discussion of this phenomenon can be found in the section 3.2.1. Overall the interface is not reactive in any form, nor does it show the formation of permanent space charge layers.

Preprints (www.preprints.org) | NOT PEER-REVIEWED | Posted: 29 July 2022 doi:10.20944/preprints202207.0443.v1

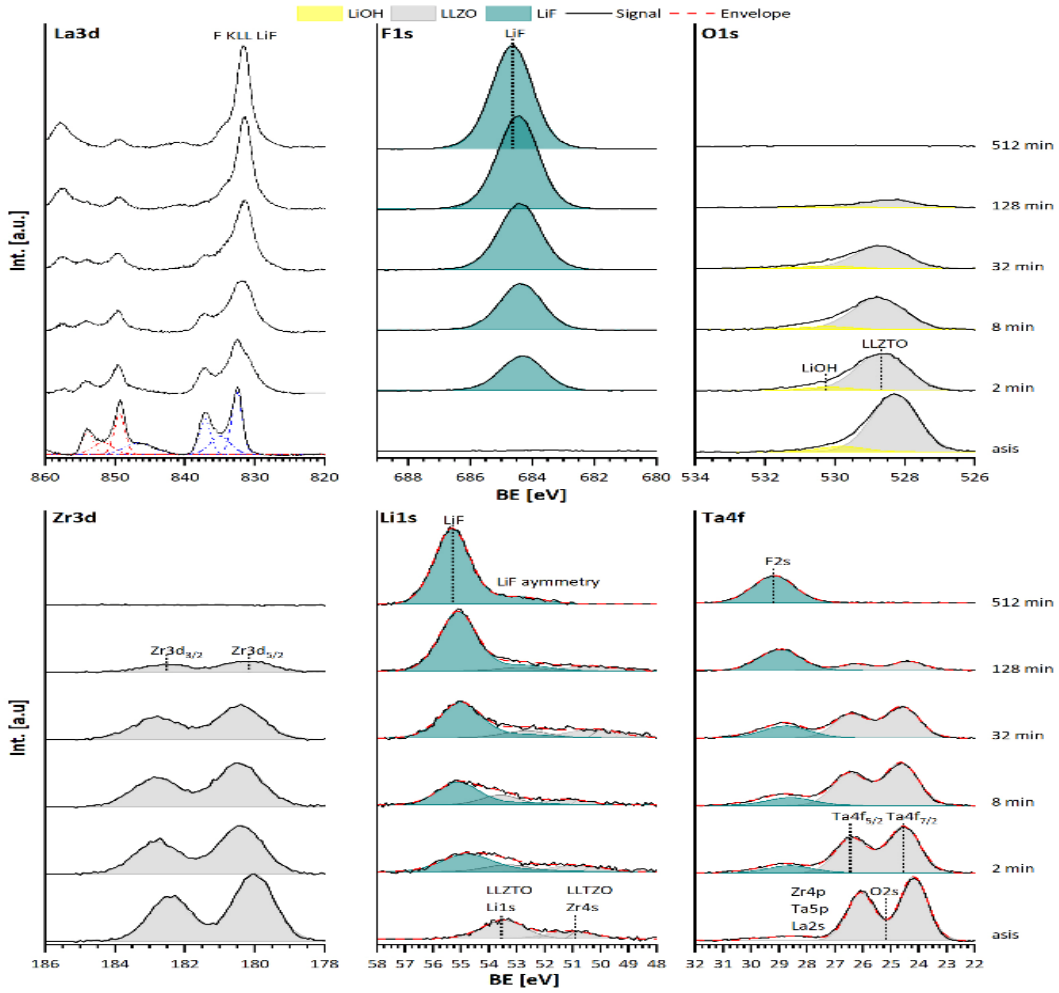

Figure 4. a) La3d, F1s, O1s, Zr3d and Ta4f XP spectra of the interface between LLZTO and LiF, where „asis" denotes the annealed LLZTO substrate deposition times of LiF from 2 min up to 512 min.

The second interface of the LiF coating to the side of the solid polymer electrolyte (SPE) is recreated with the thermal evaporation process of the oligomer PEO with a molecular weight WM = 2000 g/mol and the conductive Lithium salt LiTFSI as introduced by Ferber et al. [26] on freshly sputtered deposited LiF layer. In Figure 4 are the "asis" denoted spectra of the bare LiF layer and of the PEO+LiTFSI deposition which starts with t = 1.5 up to 24 min shown. Starting with the bare LiF layer that shows its F1s emission at E_B = 685.2 eV and Li1s emission at E_B = 56.0 eV and besides this a small amount of Li_2O is present as depicted by the emission line in the O1s spectrum at E_B = 528.3 eV [27, 28]. Neither the N1s, C1s nor the S2p spectra show any emission at all.

With the start of the PEO+LiTFSI deposition at t = 1.5 min, the F1s emission line of LiF is damped in its intensity, while a new small emission line at E_B = 688.1 eV from the CF_3 group of the LiTFSI appears [29]. The O1s spectrum now consists of three clearly distinguishable

Preprints (www.preprints.org) | NOT PEER-REVIEWED | Posted: 29 July 2022 doi:10.20944/preprints202207.0443.v1

emissions from the PEO and LiTFSI at E_B = 533.4 eV [29-31], LiOH at E_B = 531.3 eV [28, 32] and the already present Li_2O. In between there are also the emission lines for the R-O-Li and Li_2SO_3 at E_B = 531.8 and 532.2 eV as next shown from the C1s and S2p spectra [27, 33]. In the N1s spectrum there are the two emission lines from Li_3N and $Li_2NSO_2CF_3$ (as later shown) at E_B = 397.3 and 399.0 eV present [24, 28, 34]. Going further to the C1s spectrum there is the main emission line from PEO as expected at E_B = 286.5 eV accompanied by R-O-Li and hydro carbons at E_B = 285.4 and 284.7 eV [30, 31]. Lastly the S2p spectrum only exhibits the two emission lines from Li_2S and Li_2SO_3 at E_B = 160.3 and 167.8 eV [29, 33]. Already at this point it is clear, that the LiTFSI heavily reacts at the surface of the LiF, since no LiTFSI emissions are visible, but its decomposition products are. In contrast, the PEO remains mostly intact and a differentiation, whether the carbon containing products origin form LiTFSI only or LiTFSI and PEO is not straightforward. After t = 6 min, the situation did not change drastically. In the F1s spectrum the LiF and LiTFSI emissions are now equally intense, the O1s spectrum is dominated by the PEO and LiOH emission, the N1s consists mostly of Li_3N and minor amounts of LiTFSI, the C1s shows one strong emission for PEO accompanied by R-O-Li and hydrocarbons and a smaller LiTFSI emission, while the S2p mostly shows Li_2SO_3 and Li_2S, but now also Li_xS_y and $Li_2S_2O_4$ at E_B = ~163-164 eV and 165.9 eV [33, 35, 36]. After t = 24 min in the F1s spectrum there is mainly the LiTFSI emission line with a small amount of LiF, which is attributed to the X-ray beam damage of the LiTFSI in PEO and might not origin from the LiF substrate [26, 37]. The O1s spectrum is deconvoluted on the basis of the N1s, C1s and S2p spectra, consisting mainly of PEO, LiTFSI, Li_2SO_3 and LiOH emissions. For the N1s spectrum three emissions lines from Li_3N, $Li_2NSO_2CF_3$ and LiTFSI are visible. Further, the C1s spectrum shows increased amount of PEO, LiTFSI and hydrocarbons and minor amounts of LiC around binding energies of ~283 eV [24]. And finally, the S2p spectrum now shows the LiTFSI and $LiSO_2CF_3$ emission at E_B = 169.0 and 168.7 eV alongside the already present compounds [38]. Only the amount of Li_2S is drastically reduced.

Preprints (www.preprints.org) | NOT PEER-REVIEWED | Posted: 29 July 2022 doi:10.20944/preprints202207.0443.v1

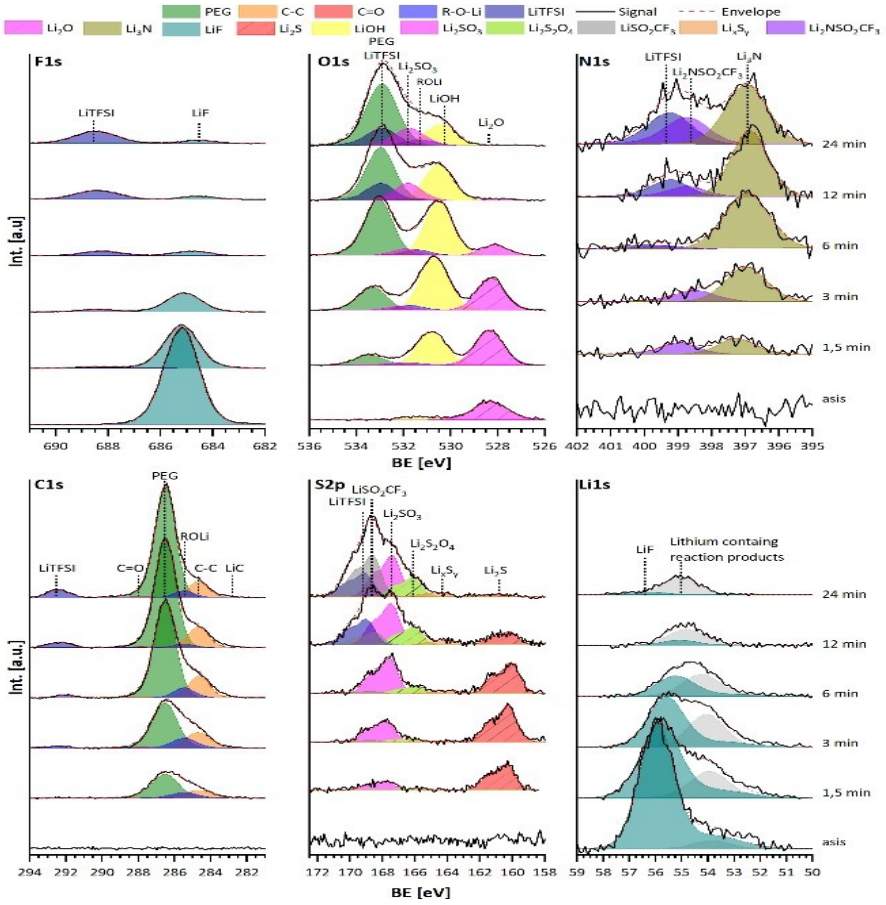

Figure 5. F1s, O1s, N1s, C1s, S2p and Li1s XP spectra of the interface between LiF and PEG+LiTFSI with deposition times from 1.5 min up to 24 min.

There are strong similarities in the kind and the order of the reaction products that are found between the here shown interface between LiF and PEO+LiTFSI and the reduction of LiTFSI on Lithium as shown by Aurbach and Yildirim [39-41]. The weakest bond in the LiTFSI is the S-N bond and when cleaved by Lithium the two segments $LiSO_2CF_3$ and $Li_2NSO_2CF_3$ form, which is indicated in the N1s and S2p spectra after t = 24 min. Also, the presence of Li_3N and Li_2S evidences the destruction of LiTFSI, as do the further products Li_2SO_3 and $Li_2S_2O_4$. Nevertheless, although the reaction products and their order hints towards a reduction reaction a direct electron transfer can be fully excluded due to the large band gap of LiF with $E_{Gap,LiF}$ = of 13.6 eV [42] and the valence band maximum around E_{VBM} = 5.9 eV.

We propose two possible pathways for the reaction, either a reaction mechanism where the LiF forms HF from the remaining water in UHV, which may be also indicated by the formation of LiOH out of Li_2O, and alternatively a further reaction of HF and LiTFSI. Alternatively, the reaction is thermodynamically driven by the large negative formation enthalpy of all the reaction

Preprints (www.preprints.org) | NOT PEER-REVIEWED | Posted: 29 July 2022 doi:10.20944/preprints202207.0443.v1

products in contrast to the LiF and LiTFSI and the surface of the LiF acts as a catalyst to initiate this reaction. Regardless of the driving force, it appears that the reaction is limited to a depth of few nanometres, since the binary Lithium salts are only found at the very interface and LiTFSI remains intact for ongoing deposition. Even though this reaction is unexpected, its impact on the functional properties might be low since the LiF layer can prevent further degradation. However, the possibility of the formation of interfacial space charge regions cannot be neglected, and will require further investigations.

3.2.1 Discussion of the binding energy shift at the LLZTO-LiF interface

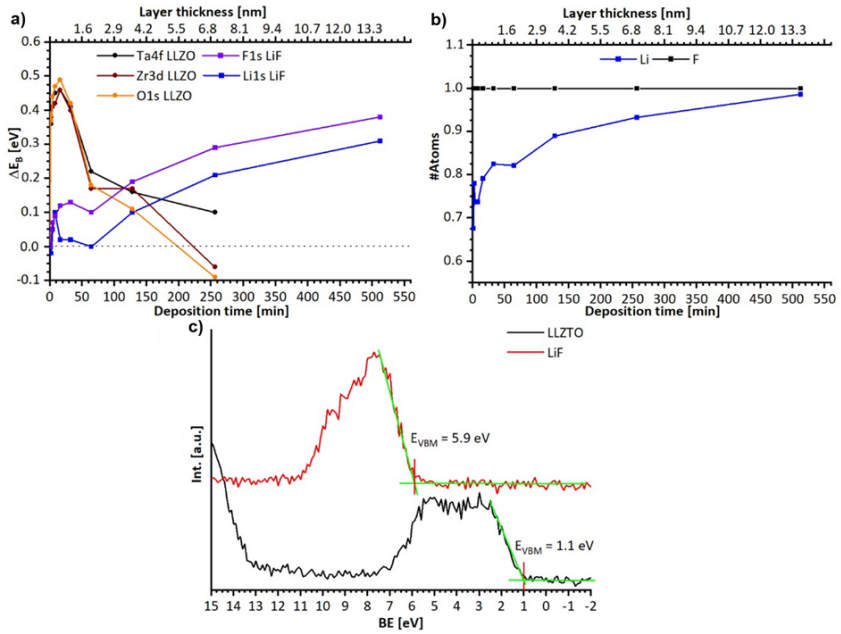

Figure 6. a) Binding energy shift observed during the LLZTO-LiF interface experiment for LLZO and LiF on the basis of the Ta4f, Zr3d and O1s position for the LLZTO and F1s and Li1s for the LiF. b) Lithium to Fluorine ration determined by XPS during the interface experimented, referenced to one Fluorine. c) Valence band spectra and EVBM position for LLZTO from the asis state and LiF after t = 512 min.

During the deposition both, the LLZTO and the LiF emission lines undergo a binding energy shift, Figure 6. While the LLZTO shifts first to higher binding energies of ΔE_B = + 0.5 eV in the first minutes of deposition and back to its original Binding energy after t = 256 min, the LiF shows only a binding energy shift to higher binding energies up to ΔE_B = + 0.3 eV after t = 512 min. After determining the layer thickness of the LiF on basis of the Lambert-Beer-Law and the damping of the LLZTO O1s, $Zr3d_{5/2}$ and $Ta4f_{7/2}$ emission line it becomes obvious, that the positive binding energy shift of the LLZTO only occurs under LiF layer thicknesses of d = 1 nm. Responsible for this behaviour is the intercalation of Li^+-cations from the plasma into the

Preprints (www.preprints.org) | NOT PEER-REVIEWED | Posted: 29 July 2022 doi:10.20944/preprints202207.0443.v1

LLZTO due the not finished forming process of the LiF. With growth of the LiF layer, the chemical potential of the Li^+-cations is lower in the LiF than in the LLZTO and the Li^+-cations are transferred back from the LLZTO into the LiF layer. Hence, a negative binding energy shift occurs in the LLZTO and a positive one in the LiF as observed. This is backed up by the Lithium to Fluorine ratio of the LiF in Figure 6b), which shows excess of Fluorine in the beginning and only forming stoichiometric LiF after t = 512 min. Any electron transfers can also be excluded by the large valence band offset of ΔE_{VBM} = 4.8 eV as measured in Figure 6c and the band gap of $E_{Gap,LiF}$ = 13.6 eV for the LiF [42].

4 Conclusions

In this work, we show that gas phase fluorination can be a viable route for the formation of a protective and well-covering surface layer on top of suitable morphologies of garnet solid electrolytes, and can be favourable compared to sputter-coating which requires UHV conditions. Applying this method to flat garnet films, we found that the surface can be well protected from degradation in ambient air under formation of Li_2CO_3. However, this method must be elaborated further to be applied to powder samples or porous pellets to understand diffusion limitations within the gas-phase. In addition, insights on the behaviour of such LiF interlayers in composite electrolytes were elaborated providing a detailed study of the interface between LLZTO as well sputter-deposited LiF, as well as LiF with deposited PEO+LiTFSI. By this, we show that LiF appears to be fully stable towards LLZTO, but it can cause side reactions to PEO+LiTFSI, which is relevant for the understanding to improve and fabricate functional composite electrolyte materials with sufficient elastic properties.

5 Conflicts of interest

There are no conflicts to declare.

6 Acknowledgements

The authors acknowledge funding by Deutsche Forschungsgemeinschaft (DFG) within CL551/3-1 and HA6128/3-1.

7 Author contributions

Conceptualization, René Hausbrand and Oliver Clemens; Funding acquisition, René Hausbrand and Oliver Clemens; Investigation, Manuel Donzelli, Thimo Ferber, Vanita Vanita, Aamir Waidha and Philipp Müller; Methodology, Manuel Donzelli, Aamir Waidha and Maximilian Mellin; Project administration, Wolfram Jaegermann; Writing – original draft, Manuel Donzelli; Writing – review & editing, Oliver Clemens.

8 References

1. R. Murugan, V. Thangadurai and W. Weppner, *Angew Chem Int Ed Engl*, 2007, **46**, 7778-7781.
2. V. Thangadurai, D. Pinzaru, S. Narayanan and A. K. Baral, *J Phys Chem Lett*, 2015, **6**, 292-299.
3. M. Fingerle, C. Loho, T. Ferber, H. Hahn and R. Hausbrand, *Journal of Power Sources*, 2017, **366**, 72-79.
4. L. Chen, Y. Li, S.-P. Li, L.-Z. Fan, C.-W. Nan and J. B. Goodenough, *Nano Energy*, 2018, **46**, 176-184.
5. Y. Li, B. Xu, H. Xu, H. Duan, X. Lu, S. Xin, W. Zhou, L. Xue, G. Fu, A. Manthiram and J. B. Goodenough, *Angew Chem Int Ed Engl*, 2017, **56**, 753-756.
6. G. Larraz, A. Orera and M. L. Sanjuan, *Journal of Materials Chemistry A*, 2013, **1**, 11419-11428.
7. A. Sharafi, S. Yu, M. Naguib, M. Lee, C. Ma, H. M. Meyer, J. Nanda, M. Chi, D. J. Siegel and J. Sakamoto, *Journal of Materials Chemistry A*, 2017, **5**, 13475-13487.
8. A. I. Waidha, T. Ferber, M. Donzelli, N. Hosseinpourkahvaz, V. Vanita, K. Dirnberger, S. Ludwigs, R. Hausbrand, W. Jaegermann and O. Clemens, *ACS Appl Mater Interfaces*, 2021, **13**, 31111-31128.
9. M. M. Besli, C. Usubelli, M. Metzger, V. Pande, K. Harry, D. Nordlund, S. Sainio, J. Christensen, M. M. Doeff and S. Kuppan, *ACS Appl Mater Interfaces*, 2020, **12**, 20605-20612.
10. H. Huo, Y. Chen, N. Zhao, X. Lin, J. Luo, X. Yang, Y. Liu, X. Guo and X. Sun, *Nano Energy*, 2019, **61**, 119-125.
11. X. Han, Y. Gong, K. K. Fu, X. He, G. T. Hitz, J. Dai, A. Pearse, B. Liu, H. Wang, G. Rubloff, Y. Mo, V. Thangadurai, E. D. Wachsman and L. Hu, *Nat Mater*, 2017, **16**, 572-579.
12. R. Dubey, J. Sastre, C. Cancellieri, F. Okur, A. Forster, L. Pompizii, A. Priebe, Y. E. Romanyuk, L. P. H. Jeurgens, M. V. Kovalenko and K. V. Kravchyk, *Advanced Energy Materials*, 2021, **11**.
13. Z. Zhang, L. Zhang, C. Yu, X. Yan, B. Xu and L.-m. Wang, *Electrochimica Acta*, 2018, **289**, 254-263.

14. S. Tang, G. Chen, F. Ren, H. Wang, W. Yang, C. Zheng, Z. Gong and Y. Yang, *Journal of Materials Chemistry A*, 2021, **9**, 3576-3583.
15. P. R. Slater, *J. Fluorine Chem.*, 2002, **117**, 43-45.
16. E. J. Moon, A. K. Choquette, A. Huon, S. Z. Kulesa, D. Barbash and S. J. May, *APL Materials*, 2015, **3**, 062511.
17. A. Nair, S. Wollstadt, R. Witte, S. Dasgupta, P. Kehne, L. Alff, P. Komissinskiy and O. Clemens, *RSC Advances*, 2019, **9**, 37136-37143.
18. C. Loho, A. J. Darbandi, R. Djenadic, O. Clemens and H. Hahn, *Chemical Vapor Deposition*, 2014, **20**, 152-160.
19. C. Loho, R. Djenadic, M. Bruns, O. Clemens and H. Hahn, *Journal of the Electrochemical Society*, 2017, **164**, A6131-A6139.
20. C. Loho, R. Djenadic, P. Mund, O. Clemens and H. Hahn, *Solid State Ionics*, 2017, **313**, 32-44.
21. S. Contarini and J. W. Rabalais, *J Electron Spectrosc*, 1985, **35**, 191-201.
22. A. I. Waidha, V. Vanita and O. Clemens, *Ceramics*, 2021, **4**, 421-436.
23. N. Schulz, R. Hausbrand, C. Wittich, L. Dimesso and W. Jaegermann, *Journal of The Electrochemical Society*, 2018, **165**, A833.
24. B. Sun, C. Xu, J. Mindemark, T. Gustafsson, K. Edström and D. Brandell, *Journal of Materials Chemistry A*, 2015, **3**, 13994-14000.
25. J. Moulder, W. Stickle, P. Sobol, K. Bomben, J. Chastain and R. King Jr, *Handbook of X-Ray Photoelectron Spectroscopy: A Reference Book of Standard Spectra for Identification and Interpretation of XPS Data*, Physical Electronics Inc. , Eden Prairie, Minn., USA, 1995.
26. T. H. Ferber, Ş. Cangaz, W. Jaegermann and R. Hausbrand, *Applied Surface Science*, 2022, **571**, 151218.
27. G. G. Eshetu, T. Diemant, S. Grugeon, R. J. r. Behm, S. Laruelle, M. Armand and S. Passerini, *ACS applied materials & interfaces*, 2016, **8**, 16087-16100.
28. K. N. Wood and G. Teeter, *ACS Applied Energy Materials*, 2018, **1**, 4493-4504.
29. D. Ensling, M. Stjerndahl, A. Nytén, T. Gustafsson and J. O. Thomas, *J. Mater. Chem.*, 2009, **19**, 82-88.
30. A. Choukourov, I. Gordeev, O. Polonskyi, A. Artemenko, L. Hanyková, I. Krakovský, O. Kylián, D. Slavínská and H. Biederman, *Plasma Processes and Polymers*, 2010, **7**, 445-458.
31. R. Dedryvère, S. Laruelle, S. Grugeon, L. Gireaud, J.-M. Tarascon and D. Gonbeau, *Journal of The Electrochemical Society*, 2005, **152**, A689.
32. K. Kanamura, S. Shiraishi, H. Tamura and Z. i. Takehara, *Journal of The Electrochemical Society*, 1994, **141**, 2379.
33. S. A. Pervez, B. P. Vinayan, M. A. Cambaz, G. Melinte, T. Diemant, T. Braun, G. Karkera, R. J. Behm and M. Fichtner, *Journal of Materials Chemistry A*, 2020, **8**, 16451-16462.
34. C. Fiedler, B. Luerssen, M. Rohnke, J. Sann and J. Janek, *Journal of the Electrochemical Society*, 2017, **164**, A3742.
35. S. Eijima, H. Sonoki, M. Matsumoto, S. Taminato, D. Mori and N. Imanishi, *Journal of The Electrochemical Society*, 2019, **166**, A5421.
36. H. D. Lim, H. Park, H. Kim, J. Kim, B. Lee, Y. Bae, H. Gwon and K. Kang, *Angewandte Chemie International Edition*, 2015, **54**, 9663-9667.
37. V. Sharova, A. Moretti, T. Diemant, A. Varzi, R. J. Behm and S. Passerini, *Journal of Power Sources*, 2018, **375**, 43-52.
38. C. C. Nguyen, S.-W. Woo and S.-W. Song, *The Journal of Physical Chemistry C*, 2012, **116**, 14764-14771.
39. D. Aurbach, I. Weissman, A. Schechter and H. Cohen, *Langmuir*, 1996, **12**, 3991-4007.
40. D. Aurbach, A. Zaban, Y. Ein-Eli, I. Weissman, O. Chusid, B. Markovsky, M. Levi, E. Levi, A. Schechter and E. Granot, *Journal of Power Sources*, 1997, **68**, 91-98.

 doi:10.20944/preprints202207.0443.v1

41. H. Yildirim, J. B. Haskins, C. W. Bauschlicher Jr and J. W. Lawson, *The Journal of Physical Chemistry C*, 2017, **121**, 28214-28234.
42. W. Tsang, C. L. Mak and K. Wong, *Applied Physics A*, 2003, **77**, 693-696.

 doi:10.20944/preprints202207.0443.v1

Supporting Information for

On the surface modification of LLZTO with LiF via a gas-phase approach and the characterization of the interfaces of LiF with LLZTO as well as PEO+LiTFSI

Manuel Donzelli[a,b], Thimo Ferber[c], Vanita Vanita[b], Aamir I. Waidha[b], Philipp Müller[c], Maximilian Mellin[c], René Hausbrand [c], Wolfram Jaegermann[c] and Oliver Clemens*[,b]

[a] *Technische Universität Darmstadt, Fachbereich Materialwissenschaft, Fachgebiet Materialdesign durch Synthese, Alarich-Weiss-Straße 2, 64287 Darmstadt, Germany.*

[b] *Universität Stuttgart, Institut für Materialwissenschaft, Chemische Materialsynthese, Heisenbergstraße 3, 70569 Stuttgart, Germany.*

[c] *Technische Universität Darmstadt, Fachbereich Materialwissenschaft, Fachgebiet Oberflächenforschung, Otto-Berndt-Straße 3, 64287 Darmstadt, Germany.*

*** Corresponding author:**

Prof. Dr. Oliver Clemens

Email: oliver.clemens@imw.uni-stuttgart.de

Fax: +49 711 685 51933

Preprints (www.preprints.org) | NOT PEER-REVIEWED | Posted: 29 July 2022 doi:10.20944/preprints202207.0443.v1

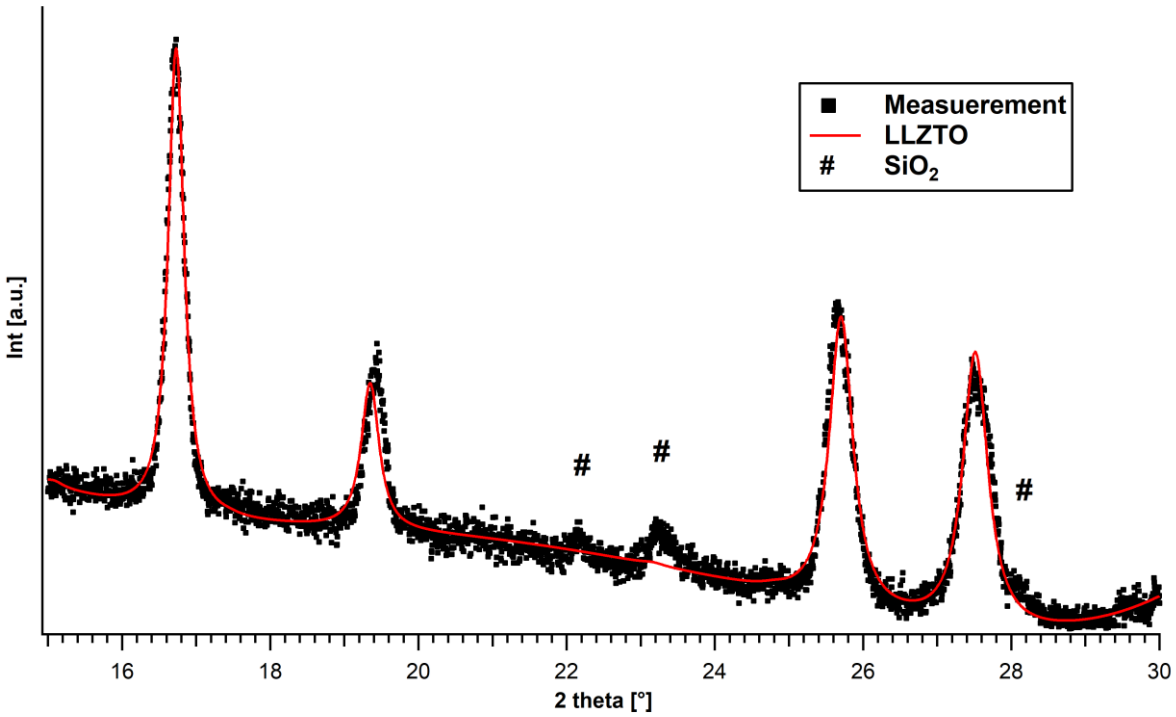

Figure S 1: XRD of the LLZTO sample coated for 5 min with LiF via gas-phase fluorination

Preprints (www.preprints.org) | NOT PEER-REVIEWED | Posted: 29 July 2022 doi:10.20944/preprints202207.0443.v1

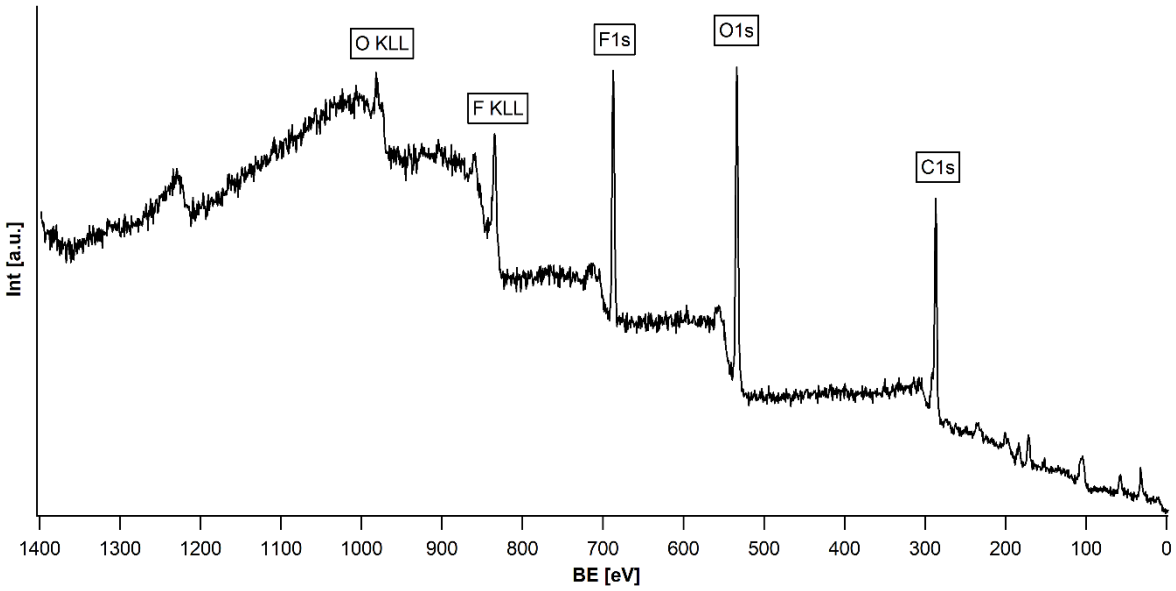

Figure S 2. XPS survey spectrum of the LLZTO film coated for 15 min with LiF via gas-phase fluorination.

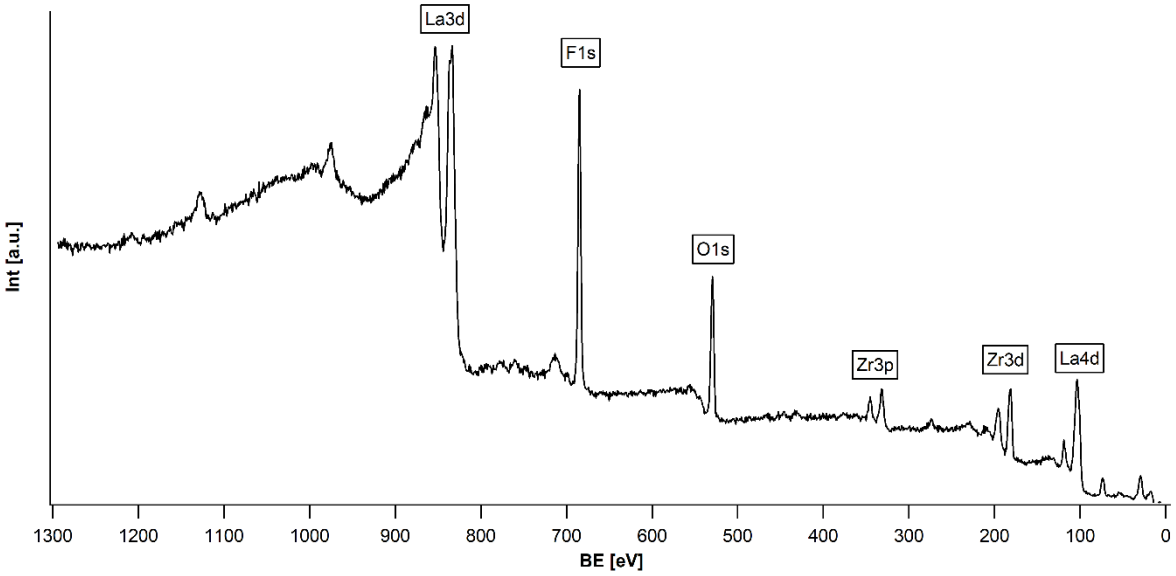

Figure S 3. XPS survey of the LLZTO coated with LiF via sputtering for 120 min

Preprints (www.preprints.org) | NOT PEER-REVIEWED | Posted: 29 July 2022 doi:10.20944/preprints202207.0443.v1

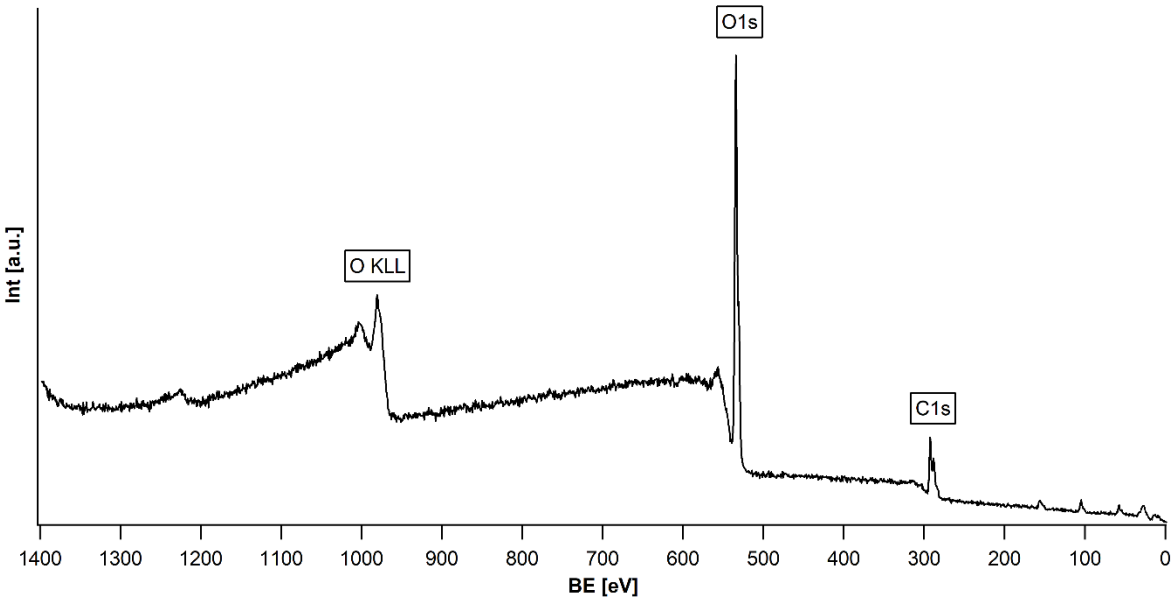

Figure S 4: XPS survey of the uncoated LLZTO sample after 24 h in air.

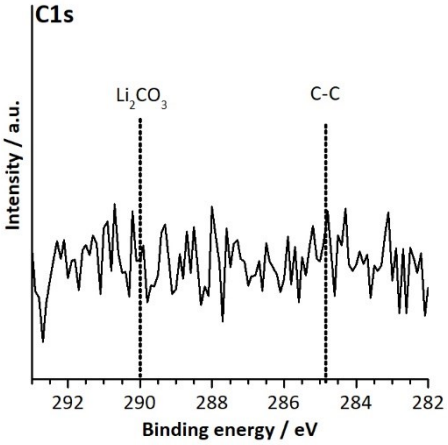

Figure S 5: C1s detailed spectrum of the annealed LLZTO surface prior to the LiF interface experiment.

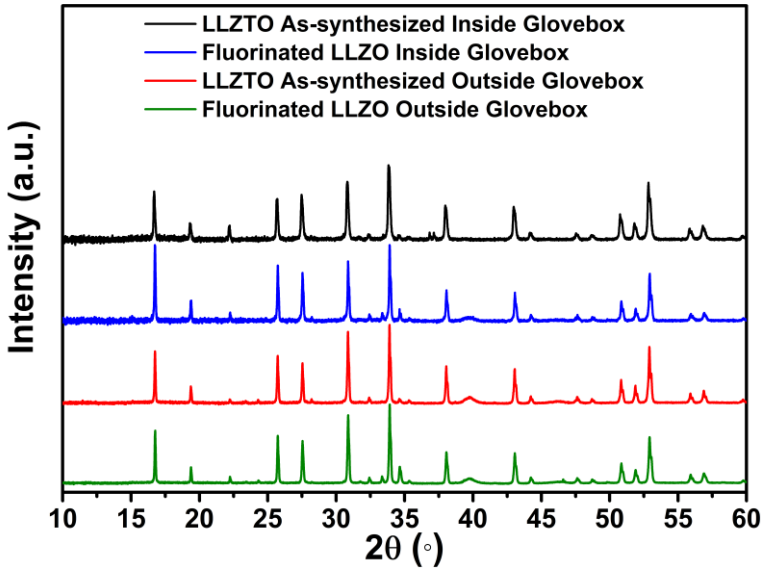

Figure S 6. Diffraction analysis of the pellet surface of LLZTO pellets before and after fluorination, as well as after exposure to ambient conditions.

Preprints (www.preprints.org) | NOT PEER-REVIEWED | Posted: 29 July 2022 doi:10.20944/preprints202207.0443.v1

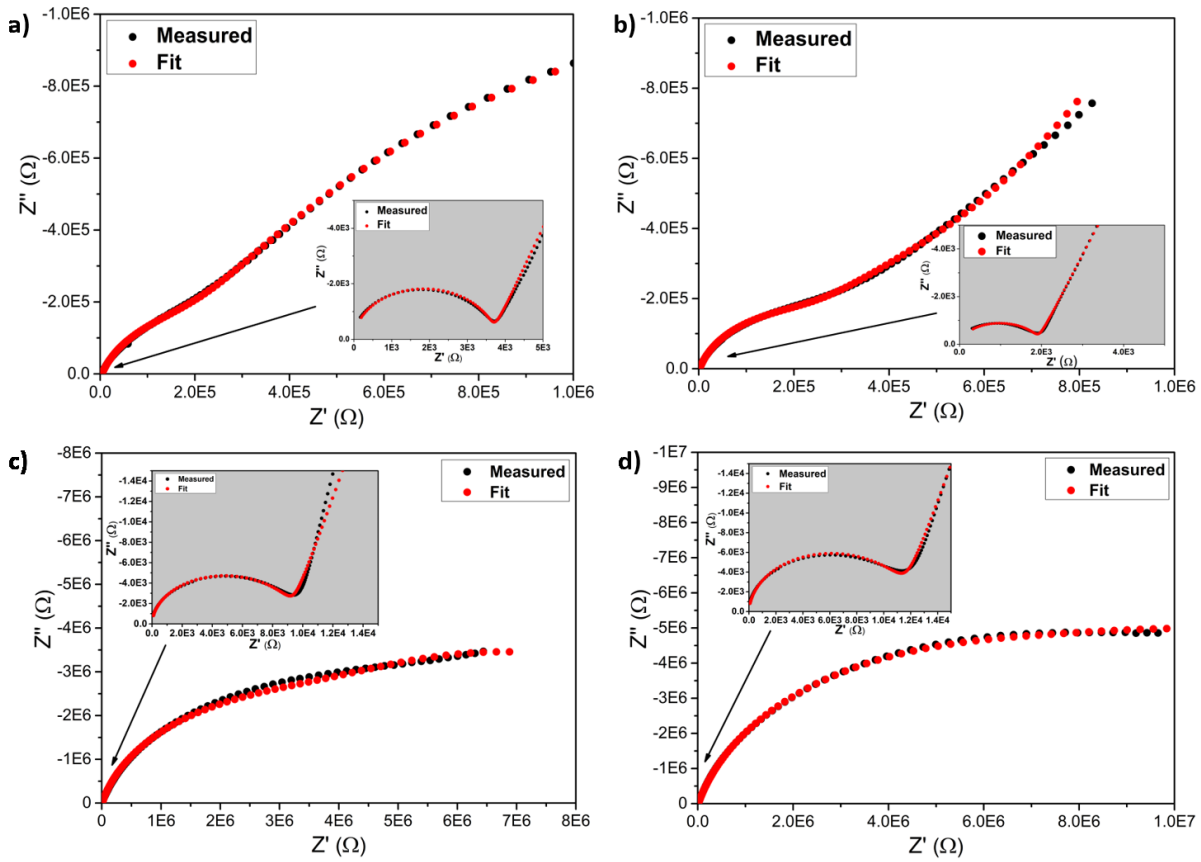

Figure S 7. Fits of the Nyquist plot recorded at 30 °C a) & b) As-synthesized and fluorinated LLZO kept inside of the glove box, c & d) As-synthesized and fluorinated LLZO kept outside of the glove box.

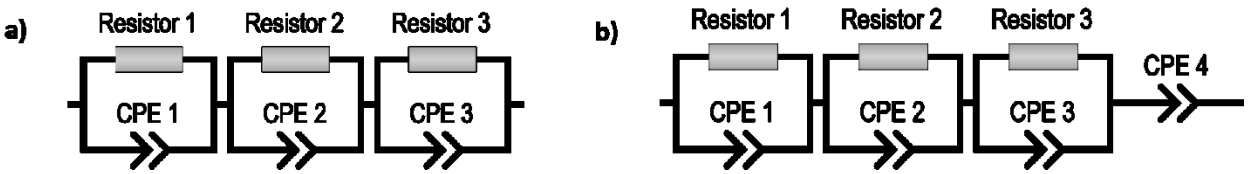

Figure S 8. Equivalent circuit models used for the evaluation of impedance data shown in Figure 6 and Figure S 7. a) was used for the modelling the impedance data for the as-synthesized LLZTO pellet inside the glove box and also for both the as-synthesized and fluorinated LLZO pellet outside of the glovebox. b) was used for fitting the impedance data of the fluorinated LLZTO pellets kept inside of the glove box.